Polarimetric SAR Image Filtering Based on Patch Ordering and Simultaneous Sparse Coding

Bin Xu, Yi Cui, *Member, IEEE*, Bin Zuo, Jian Yang, *Senior Member, IEEE*, and Jianshe Song

***Abstract*—In this paper, a transform-domain filtering method is proposed for polarimetric synthetic aperture radar (POLSAR) images via patch ordering and simultaneous sparse coding (SSC). First of all, we establish a signal-dependent additive noise model for the POLSAR covariance matrix and derive the noise variance for each element of the matrix based on the complex Wishart distribution. Next, we propose an extended patch ordering algorithm for POLSAR images by extracting sliding patches and organizing them in a regular way. Then, the ordered patches are filtered by SSC, for the purpose of which we develop a new weighted simultaneous orthogonal matching pursuit algorithm by embedding the signal-dependent noise model of the POLSAR data. Finally, the filtering result is reconstructed from the filtered patches via inverse permutation and subimage averaging. Experimental results with both simulated and real POLSAR images demonstrate that the proposed method can achieve state-of-the-art filtering performance.**

***Index Terms*—Patch ordering, polarimetric synthetic aperture radar (POLSAR), simultaneous sparse coding (SSC), speckle filtering.**

I. Introduction

POLARIMETRIC synthetic aperture radar (POLSAR) is a very important microwave remote sensing technique which is capable of acquiring a high-resolution and multidimensional image of the earth terrain in different wave polarization channels. However, the applications of POLSAR are often affected by a noiselike phenomenon, called speckle, as originated from its coherent imaging nature. During the past years, many methods have been proposed to reduce the speckle in POLSAR imagery. The boxcar filter is widely used because of its simplicity. However, its performance has not been satisfying due to indiscriminate averaging. Lee *et al.* [1], [2] used the minimum-mean-square-error criterion to filter the covariance or coherency matrices. In the refined Lee filter [2], the pixels in edged aligned windows are selected for weighted averaging. Unlike the refined Lee filter, the intensity-driven adaptive-neighborhood (IDAN) filter [3] selects a group of stationary pixels surrounding the estimated pixel by using the diagonal elements of the covariance or coherency matrices. To obtain homogeneous pixels effectively, the scattering model-based filter [4] selects the pixels which correspond to the same scattering mechanism as the estimated pixel in a square window. Other classical filters also include the model-based POLSAR filter [5] which is on the basis of the multiplicative–additive speckle noise model [6], the subspace decomposition-based filter [7], the trace-based filter [8], and so on.

The nonlocal means (NLM) algorithm [9] provides a new way to tackle the filtering problem, and this method has been extended to POLSAR image filtering. Deledalle *et al.* adapted the probabilistic patch-based algorithm [10] proposed in SAR image despeckling to POLSAR imagery and proposed the nonlocal framework for SAR denoising (NLSAR) [11]. Chen *et al.* [12] proposed the NLM-pretest filter by using the test statistic [13] in the complex Wishart distribution. Torres *et al.* [14] proposed the SDNLM filter with stochastic distances. Liu and Zhong [15] proposed the NLM-DSM filter based on discriminative similarity measure. All these methods adopt the framework of the NLM but use different similarity measurements.

Most recently, advances in state-of-the-art signal processing techniques, particularly the sparse representation [16]–[18], have opened an exciting new vision for image denoising. In [16], Elad and Aharon proposed a novel image filtering method using sparse representations over learned dictionaries. Then, this method was adapted to color image filtering [17]. In [18], Mairal *et al.* combined the nonlocal method and simultaneous sparse coding (SSC) and then proposed the nonlocal sparse model. Sparse representation has already been used for despeckling single-channel SAR images [19]–[21]. In our previous work [21], we proposed a SAR image filtering method which is based on SSC, wavelet transform, and patch ordering, a newly proposed scheme by Ram *et al.* [22]. However, to the best of our knowledge, applying sparse representation to POLSAR image filtering still remains a challenging problem, and very few works have been previously reported toward this purpose. There are probably twofold reasons. On the one hand, SAR speckle is intrinsically of multiplicative nature such that the noise level is no longer independent of the underlying signal. On the other hand, POLSAR data have multiple channels, and the speckle not only appears in respective intensity images but is also present in their complex correlation. Such a fact invalidates the common approach of logarithmic transformation which only transforms the multiplicative noise of the real intensity into an additive one.

Manuscript received June 6, 2014; revised March 30, 2015, September 6, 2015, November 21, 2015, and January 11, 2016; accepted February 27, 2016. Date of publication March 21, 2016; date of current version May 24, 2016. This work was supported in part by the National Natural Science Foundation of China (NSFC) under Grant 41171317, by the Key Project of the NSFC under Grant 61132008, by the Major Research Plan of the NSFC under Grant 61490693, and by the Aviation Research Foundation.

B. Xu, B. Zuo, and J. Yang are with the Department of Electronic Engineering, Tsinghua University, Beijing 100084, China (e-mail: xubin07161@gmail.com; zuob2009@126.com; yangjian_ee@mail.tsinghua.edu.cn).

Y. Cui was with the Global Institute for Collaborative Research and Education, Hokkaido University, Sapporo 060-0808, Japan. He is now with Stanford University, Palo Alto, CA 94304 USA (e-mail: cuiyi.trea@gmail.com).

J. Song is with the Xi'an Research Institute of Hi-Technology, Xi'an 710025, China (e-mail: Songjianshe09@126.com).

Color versions of one or more of the figures in this paper are available online at http://ieeexplore.ieee.org.

Digital Object Identifier 10.1109/TGRS.2016.2536648

This paper is therefore dedicated as a first attempt for POLSAR image filtering using sparse representation. It is also based on patch ordering and SSC, which have already been used in our previous work [21]. However, the proposed method is different from our previous work [21] in the following three aspects. First, unlike the logarithmic transformation used in [21], we adopt a signal-dependent additive noise model for the full POLSAR data based on the complex Wishart distribution. Second, the original patch ordering algorithm is extended to POLSAR images based on the test statistic in the complex Wishart distribution. Third, we perform transform-domain filtering via simultaneous sparse representation for nonuniform noise due to the nature of the speckle in POLSAR imagery.

The rest of this paper is organized as follows. Section II presents the POLSAR data statistics and the additive noise model. Section III presents the patch ordering for POLSAR images and SSC for nonuniform noise. Section IV describes the proposed algorithm and parameter selection. Section V reports the experimental results. Section VI discusses the effect of strong point detection, several parameters, and time consumption. Finally, Section VII concludes this paper.

II. POLSAR Data Statistics and Additive Noise Model

A. POLSAR Data

A single-look POLSAR data set measures, for each resolution cell (pixel), the Sinclair scattering matrix, which is a 2×2 complex matrix. In the linear horizontal and vertical polarization base, this matrix can be expressed by

$$\mathbf{S} = \begin{bmatrix} S_{\mathrm{hh}} & S_{\mathrm{hv}} \\ S_{\mathrm{vh}} & S_{\mathrm{vv}} \end{bmatrix}. \tag{1}$$

Here, S_{kl} stands for the scattering coefficient of k-transmitting and l-receiving polarizations. In general, the reciprocity holds, and the scattering matrix is symmetrical, i.e., $S_{\mathrm{hv}} = S_{\mathrm{vh}}$. Then, in the single-look case, the scattering information can be also represented by a complex vector

$$\mathbf{u} = \begin{bmatrix} S_{\mathrm{hh}} & \sqrt{2}S_{\mathrm{hv}} & S_{\mathrm{vv}} \end{bmatrix}^T \tag{2}$$

where the superscript "^{T}" stands for the transpose. In the multilook case, the scattering information can be represented by the covariance matrix $\mathbf{C}$

$$\begin{aligned} \mathbf{C} &= \langle \mathbf{u}\mathbf{u}^H \rangle \\ &= \begin{bmatrix} \langle |S_{\mathrm{hh}}|^2 \rangle & \langle \sqrt{2}S_{\mathrm{hh}}S_{hv}^* \rangle & \langle S_{\mathrm{hh}}S_{\mathrm{vv}}^* \rangle \\ \langle \sqrt{2}S_{\mathrm{hv}}S_{\mathrm{hh}}^* \rangle & \langle 2|S_{\mathrm{hv}}|^2 \rangle & \langle \sqrt{2}S_{\mathrm{hv}}S_{\mathrm{vv}}^* \rangle \\ \langle S_{\mathrm{vv}}S_{\mathrm{hh}}^* \rangle & \langle \sqrt{2}S_{\mathrm{vv}}S_{\mathrm{hv}}^* \rangle & \langle |S_{\mathrm{vv}}|^2 \rangle \end{bmatrix} \end{aligned} \tag{3}$$

where "$\langle\cdot\rangle$" is the ensemble average, the superscript "^{H}" is the conjugate transpose, and the superscript "*" is the complex conjugate. The SPAN (or total power) is expressed as

$$\mathrm{SPAN} = \mathrm{Tr}(\mathbf{C}) \tag{4}$$

where $\mathrm{Tr}()$ is the trace of a matrix.

It is well established that, with finite-look averaging, the covariance matrix follows the complex Wishart distribution [23], [24]

$$p_{\mathbf{C}}(\mathbf{C}) = \frac{L^{qL}|\mathbf{C}|^{L-q}\exp\left[-L\mathrm{Tr}(\mathbf{\Sigma}^{-1}\mathbf{C})\right]}{K(L,q)|\mathbf{\Sigma}|^L} \tag{5}$$

where L is the equivalent number of looks (ENL), q is the dimension of $\mathbf{u}$, $\mathbf{\Sigma}$ is the expectation of $\mathbf{C}$, and K is a normalization factor. It should be noted that the ENL can be easily estimated from a homogeneous region by [25]

$$\hat{L} = \frac{\mathrm{Tr}\left(\langle \mathbf{C} \rangle\right)^2}{\langle \mathrm{Tr}(\mathbf{C}\mathbf{C}) \rangle - \mathrm{Tr}\left(\langle \mathbf{C} \rangle \langle \mathbf{C} \rangle\right)}. \tag{6}$$

B. Additive Noise Model

The purpose of POLSAR filtering is to reconstruct $\mathbf{\Sigma}$ from the noisy observable $\mathbf{C}$. The speckle statistics depends on the complex correlation coefficient, and the noise statistics of the off-diagonal terms is different from that of the diagonal terms. Thus, how to denoise the off-diagonal terms of $\mathbf{C}$ is a challenging topic in POLSAR image filtering. In this paper, we adopt an additive noise model which regards the speckle as a signal-dependent additive noise.

In general, the diagonal terms of $\mathbf{C}$ can be characterized by the multiplicative noise model [23]. For example

$$\mathbf{C}_{11} = \mathbf{\Sigma}_{11} w \tag{7}$$

where w is characterized by unit-mean gamma distribution. Furthermore, (7) can be also written in an additive but signal-dependent way [26], [27]

$$\mathbf{C}_{11} = \mathbf{\Sigma}_{11} + \mathbf{Z}_{11} \tag{8}$$

where $\mathbf{Z}_{11}$ is the signal-dependent additive noise of $\mathbf{C}_{11}$

$$\mathbf{Z}_{11} = \mathbf{\Sigma}_{11}(w-1). \tag{9}$$

The off-diagonal terms of $\mathbf{C}$ are characterized by a combination of the additive and multiplicative noise model [6] and can also be written in the same way as shown in (8). Thus, we have

$$\mathbf{C} = \mathbf{\Sigma} + \mathbf{Z} \tag{10}$$

where $\mathbf{Z}$ is the signal-dependent additive noise of $\mathbf{C}$.

Here, $\mathbf{Z}$ has zero mean. The variances of the diagonal terms of $\mathbf{Z}$ are

$$\mathrm{var}[\mathbf{Z}_{kk}] = \frac{\mathbf{\Sigma}_{kk}^2}{L}. \quad (k = 1, 2, 3). \tag{11}$$

The variances of the off-diagonal terms of $\mathbf{Z}$ are

$$\begin{aligned} \mathrm{var}\left[\mathrm{Re}(\mathbf{Z}_{kl})\right] &= \frac{1}{2L}\left[\mathrm{Re}(\mathbf{\Sigma}_{kl})^2 - \mathrm{Im}(\mathbf{\Sigma}_{kl})^2 + \mathbf{\Sigma}_{kk}\mathbf{\Sigma}_{ll}\right] \\ \mathrm{var}\left[\mathrm{Im}(\mathbf{Z}_{kl})\right] &= \frac{1}{2L}\left[\mathrm{Im}(\mathbf{\Sigma}_{kl})^2 - \mathrm{Re}(\mathbf{\Sigma}_{kl})^2 + \mathbf{\Sigma}_{kk}\mathbf{\Sigma}_{ll}\right]. \\ & (k,l) \in \{(1,2),(1,3),(2,3)\}. \end{aligned} \tag{12}$$

The derivations of (11) and (12) can be found in [28]. In Appendix A, we also present the derivations of (11) and (12) in a new way by using the characteristic function [24].

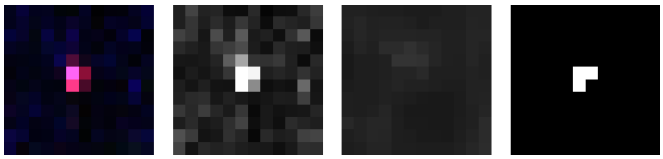

(a) (b) (c) (d)

Fig. 1. Example of strong isolated point detection. (a) 12×12 POLSAR image patch. (b) SPAN of (a). (c) SPAN_{med} of (a). $B_2 = 5$. (d) Detection result of (a). $\lambda = 5$.

Thus, if we have $\mathbf{\Sigma}$, we can estimate the noise variance. An intuitive way to estimate $\mathbf{\Sigma}$ is applying a $B_1 \times B_1$ boxcar filter to the input POLSAR image. However, the noise variance will be overestimated around strong isolated points. To avoid the overestimation, the values of strong isolated points are set to zeros before the noise variance estimation. In this way, the noise variance around strong isolated points will be underestimated. Thus, we can get good point target preserving ability which will be shown in Section V.

To detect strong isolated points, we first apply a $B_2 \times B_2$ median filter to the SPAN of the input POLSAR image. Let SPAN_{med} be the median filtering result. Then, a pixel is considered as strong isolated points if

$$\frac{\text{SPAN}}{\text{SPAN}_{\text{med}}} > \lambda \tag{13}$$

where λ is a predefined threshold. In this paper, $B_1 = 5$, $B_2 = 5$, and $\lambda = 5$ (for the detail of parameter selection, please refer to Section IV). Fig. 1 presents an example of strong isolated point detection. Fig. 1(b) and (c) are the SPAN and SPAN_{med} of Fig. 1(a), respectively. Strong pixels are removed in Fig. 1(c). Thus, (13) can be used to detect strong points. In Fig. 1(d), we can also find that strong isolated pixels are well detected.

Suppose that the matrices $\mathbf{C}$, $\mathbf{\Sigma}$, and $\mathbf{Z}$ can be respectively rewritten in the vector form as (14)–(16), shown at the bottom of the page.

Thus, we can treat each pixel of the POLSAR image as a 1×9 vector. Then, the additive noise model can be rewritten as follows:

$$\mathbf{c} = \mathbf{s} + \mathbf{z}. \tag{17}$$

This additive noise model is adopted in the subsequent filtering method.

III. Patch Ordering and SSC

A. Patch Ordering for POLSAR Images

For an $N_1 \times N_2$ POLSAR image, we extract the sliding patches of size $n \times n$. The number of patches is

$$N^{(p)} = \left(\left\lceil \frac{N_1 - n}{SL} \right\rceil + 1 \right) \left(\left\lceil \frac{N_2 - n}{SL} \right\rceil + 1 \right) \tag{18}$$

where SL is the sliding step and $\lceil \cdot \rceil$ is the ceil function.

Based on the test statistic [13] in the complex Wishart distribution, Chen *et al.* [12] derived the similarity of two patches $\mathbf{P}_1(i)$ $(i = 1, 2, \ldots, n^2)$ and $\mathbf{P}_2(i)$ $(i = 1, 2, \ldots, n^2)$

$$H = \sum_{i=1}^{n^2} \left(\ln |\mathbf{P}_1(i)| + \ln |\mathbf{P}_2(i)| - 2 \ln |\mathbf{P}_1(i) + \mathbf{P}_2(i)| \right). \tag{19}$$

It should be noted that the determinant of a covariance matrix may be zero when $L \leq 2$. In this case, (19) makes no sense. To solve this problem, we first apply a 3×3 boxcar filter to the input POLSAR image. Then, we use the boxcar filtering result I_B to calculate the similarity of two patches.

As stated in [21] and [22], patch ordering aims to reorder the sliding patches by using the similarity between the patches. The similarity between neighboring ordered patches is very high; thus, SSC is very suitable for ordered patches. The original patch ordering method [22] proposed for additive white Gaussian noise can be easily adapted to POLSAR images by replacing the Euclidean distance with (19). The patch ordering algorithm for POLSAR images is given in Algorithm 1.

Algorithm 1 Patch ordering algorithm for POLSAR images.

Input: The image patches $\mathbf{P}_k$ $(k = 1, \ldots, N^{(p)})$.
Parameter: The search range $R \times R$.
  Set the first patch to be the initial patch, i.e., $\Omega(1) = 1$.
  for $k = 1$ to $N^{(p)} - 1$ **do**
    Let $\mathbf{P}_{\Omega(k)}$ and SR_k be the current patch and the set of indices of the search range around $\mathbf{P}_{\Omega(k)}$, respectively.
    if $|SR_k \setminus \Omega| \geq 1$,[1] **then**
      Calculate the similarity of $\mathbf{P}_l$ and $\mathbf{P}_{\Omega(k)}$ by (19), where $l \in SR_k \setminus \Omega$. Choose the patch $\mathbf{P}_{\hat{l}}$ which is the most similar to $\mathbf{P}_{\Omega(k)}$.
    else
      Choose the spatially nearest patch $\mathbf{P}_{\hat{l}}$ to $\mathbf{P}_l$.
    end if
    $\Omega(k+1) = \hat{l}$
  end for
Output: The set Ω which holds the ordering.

Since each pixel of the POLSAR image can be treated as a 1×9 vector, the $n \times n$ patch can be considered as nine $n^2 \times 1$ vectors $\mathbf{q}_i$ $(i = 1, \ldots, 9)$ or $n^2 \times 9$ matrix $\mathbf{Q}$

$$\mathbf{Q} = [\mathbf{q}_1 \quad \cdots \quad \mathbf{q}_9]. \tag{20}$$

Let $\mathbf{X}$ and $\mathbf{Y}$ be the patches before and after patch ordering, respectively

$$\mathbf{X} = \left[\mathbf{Q}_1 \quad \cdots \quad \mathbf{Q}_{N^{(p)}} \right] \tag{21}$$

$$\mathbf{Y} = \left[\mathbf{Q}_1^{(p)} \quad \cdots \quad \mathbf{Q}_{N^{(p)}}^{(p)} \right]. \tag{22}$$

[1]Here, $|\cdot|$ is the number of elements within a set and "\" is the set difference.

$$\mathbf{c} = \left[\mathbf{C}_{11} \quad \mathbf{C}_{22} \quad \mathbf{C}_{33} \quad \text{Re}(\mathbf{C}_{12}) \quad \text{Re}(\mathbf{C}_{13}) \quad \text{Re}(\mathbf{C}_{23}) \quad \text{Im}(\mathbf{C}_{12}) \quad \text{Im}(\mathbf{C}_{13}) \quad \text{Im}(\mathbf{C}_{23}) \right] \tag{14}$$

$$\mathbf{s} = \left[\mathbf{\Sigma}_{11} \quad \mathbf{\Sigma}_{22} \quad \mathbf{\Sigma}_{33} \quad \text{Re}(\mathbf{\Sigma}_{12}) \quad \text{Re}(\mathbf{\Sigma}_{13}) \quad \text{Re}(\mathbf{\Sigma}_{23}) \quad \text{Im}(\mathbf{\Sigma}_{12}) \quad \text{Im}(\mathbf{\Sigma}_{13}) \quad \text{Im}(\mathbf{\Sigma}_{23}) \right] \tag{15}$$

$$\mathbf{z} = \left[\mathbf{Z}_{11} \quad \mathbf{Z}_{22} \quad \mathbf{Z}_{33} \quad \text{Re}(\mathbf{Z}_{12}) \quad \text{Re}(\mathbf{Z}_{13}) \quad \text{Re}(\mathbf{Z}_{23}) \quad \text{Im}(\mathbf{Z}_{12}) \quad \text{Im}(\mathbf{Z}_{13}) \quad \text{Im}(\mathbf{Z}_{23}) \right] \tag{16}$$

Then, the subsequent filtering method will work on the ordered patches $\mathbf{Y}$.

B. Filtering via SSC

1) Sparse Coding: Sparse coding [16] is very useful in image filtering. It assumes that the clean signal can be represented by a linear combination of few atoms in a redundant dictionary. The sparse model [16] for uniform noise is

$$\min_{\boldsymbol{\alpha}_i} \|\boldsymbol{\alpha}_i\|_0 \ \text{ s.t. } \ \|\mathbf{y}_i - \mathbf{D}\boldsymbol{\alpha}_i\|_2^2 \le n^2(\gamma\sigma)^2 \tag{23}$$

where the size of the patch is $n \times n$, $\mathbf{y}_i \in \mathbb{R}^{n^2}$ is the column vector in $\mathbf{Y}$ and stands for the noisy signal, $\mathbf{D} \in \mathbb{R}^{n^2 \times K} (K > n^2)$ is an overcomplete dictionary, $\boldsymbol{\alpha}_i \in \mathbb{R}^K$ is the sparse representation of $\mathbf{y}_i$, σ is the noise standard deviation, and γ is a predefined parameter controlling the depth of filtering. The sparse coding problem (23) can be solved by the orthogonal matching pursuit (OMP) algorithm [29], and the filtering result of $\mathbf{y}_i$ is

$$\hat{\mathbf{y}}_i = \mathbf{D}\hat{\boldsymbol{\alpha}}_i. \tag{24}$$

In general, most of the image filtering methods are designed for uniform noise. However, from (11) and (12), we can find that the noise is nonuniform for POLSAR images. Thus, we should adopt the sparse model [17] for nonuniform noise

$$\min_{\boldsymbol{\alpha}_i} \|\boldsymbol{\alpha}_i\|_0 \ \text{ s.t. } \ \left\| \frac{1}{\boldsymbol{\sigma}_i} \otimes (\mathbf{y}_i - \mathbf{D}\boldsymbol{\alpha}_i) \right\|_2^2 \le n^2\gamma^2 \tag{25}$$

where $\boldsymbol{\sigma}_i \in \mathbb{R}^{n^2}$ is the noise standard deviation corresponding to $\mathbf{y}_i$, $1/\boldsymbol{\sigma}_i$ is the elementwise reciprocal of $\boldsymbol{\sigma}_i$, and $\otimes$ denotes the elementwise multiplication between two vectors. This problem can also be solved by the OMP algorithm.

In fact, the problem (23) can be written in the following form:

$$\min_{\boldsymbol{\alpha}_i} \|\boldsymbol{\alpha}_i\|_0 \ \text{ s.t. } \ \left\| \frac{1}{\sigma}(\mathbf{y}_i - \mathbf{D}\boldsymbol{\alpha}_i) \right\|_2^2 \le n^2\gamma^2. \tag{26}$$

Thus, we can easily obtain the sparse model for nonuniform noise from the uniform case by replacing $(1/\sigma)(\mathbf{y}_i - \mathbf{D}\boldsymbol{\alpha}_i)$ with $(1/\boldsymbol{\sigma}_i) \otimes (\mathbf{y}_i - \mathbf{D}\boldsymbol{\alpha}_i)$.

2) SSC: The core idea of SSC is that several similar signals can be represented by different linear combinations of the same atoms. For uniform noise, denoising several similar signals $\mathbf{y}_i$ $(i \in G)$ amounts to solving

$$\min_{\boldsymbol{\Lambda}} \|\boldsymbol{\Lambda}\|_{0,\infty} \text{ s.t. } \sum_{i \in G} \|\mathbf{y}_i - \mathbf{D}\boldsymbol{\alpha}_i\|_2^2 \le mn^2(\gamma\sigma)^2 \tag{27}$$

where G is the group of similar signals, m is the number of signals in set G, $\boldsymbol{\Lambda}$ is

$$\boldsymbol{\Lambda} = (\cdots \boldsymbol{\alpha}_i \cdots)_{i \in G} \tag{28}$$

and $\|\boldsymbol{\Lambda}\|_{0,\infty}$ is a pseudonorm [30] which denotes the number of nonzero rows of $\boldsymbol{\Lambda}$. For POLSAR images, each patch can be considered as nine correlated signals. Since these correlated signals are acquired in the same region, they have high similarity. Moreover, the similarity of neighboring patches in $\mathbf{Y}$ is also very high. Thus, we use $N^{(G)}$ neighboring patches to form a group, and each group has $9N^{(G)}$ signals, i.e., $m = 9N^{(G)}$. The SSC problem (27) can be solved by the simultaneous OMP (S-OMP) algorithm [30], [31].

In the same way, the simultaneous sparse model for nonuniform noise is

$$\min_{\boldsymbol{\Lambda}} \|\boldsymbol{\Lambda}\|_{0,\infty} \text{ s.t. } \sum_{i \in G} \left\| \frac{1}{\boldsymbol{\sigma}_i} \otimes (\mathbf{y}_i - \mathbf{D}\boldsymbol{\alpha}_i) \right\|_2^2 \le mn^2\gamma^2. \tag{29}$$

To solve this problem, we just need to modify the S-OMP algorithm with the consideration of $\boldsymbol{\sigma}_i$. The detail of the modified S-OMP algorithm is shown in Algorithm 2. The modification is very simple, and we will not go deep into the discussion of this modification. Since the noise in POLSAR images is nonuniform, we will use the simultaneous sparse model for nonuniform noise to filter the noisy patches $\mathbf{Y}$.

Algorithm 2 The modified S-OMP algorithm.

Task: Approximate the solution of (29).
Input: The dictionary $\mathbf{D} = [\mathbf{d}_1, \ldots, \mathbf{d}_K]$, the signals $\mathbf{y}_i$ $(i = 1, \ldots, m)$, the noise standard deviation $\boldsymbol{\sigma}_i$ $(i = 1, \ldots, m)$ corresponding to $\mathbf{y}_i$.
Initialization: Initialize $l = 0$, and set
the initial solution $\boldsymbol{\alpha}_i^0 = \mathbf{0}$ $(i = 1, \ldots, m)$,
the initial solution support $\Omega^0 = \text{Support}\{\boldsymbol{\alpha}_1^0\} = \emptyset$,
the initial residual $\mathbf{r}_i^0 = (1/\boldsymbol{\sigma}_i) \otimes \mathbf{y}_i$ $(i = 1, \ldots, m)$.
Main Iteration:
while $\sum_{i=1}^m \|\mathbf{r}_i^l\|_2^2 > mn^2$ **do**
for $k = 1$ to K **do**
for $i = 1$ to m **do**
$\hat{\mathbf{d}}_k = \boldsymbol{\sigma}_i \otimes \mathbf{d}_k$.
Compute the error $\varepsilon(k,i) = \min_t \|\hat{\mathbf{d}}_k t - \mathbf{r}_i^l\|_2^2$ using the optimal choice $t = \hat{\mathbf{d}}_k^T \mathbf{r}_i^l / \|\hat{\mathbf{d}}_k\|_2^2$.
end for
Compute the error $\varepsilon'(k) = \sum_{i=1}^m \varepsilon(k,i)$.
end for
$l \Leftarrow l + 1$.
$\hat{k} = \arg\min_k \varepsilon'(k)$, and update $\Omega^l = \Omega^{l-1} \cup \{\hat{k}\}$.
for $i = 1$ to m **do**
for $k = 1$ to K **do**
$\hat{\mathbf{d}}_k = \boldsymbol{\sigma}_i \otimes \mathbf{d}_k$.
end for
Get the new dictionary $\hat{\mathbf{D}} = [\hat{\mathbf{d}}_1, \ldots, \hat{\mathbf{d}}_K]$, and update the solution,
$\boldsymbol{\alpha}_i^l = \arg\min_{\boldsymbol{\alpha}_i} \|(1/\boldsymbol{\sigma}_i) \otimes \mathbf{y}_i - \hat{\mathbf{D}}\boldsymbol{\alpha}_i\|_2^2$ s.t. Support $\{\boldsymbol{\alpha}_i\} = \Omega^l$.
Update the residual $\mathbf{r}_i^l = (1/\boldsymbol{\sigma}_i) \otimes (\mathbf{y}_i - \mathbf{D}\boldsymbol{\alpha}_i^l)$.
end for
end while
Get the final result $\hat{\boldsymbol{\alpha}}_i = \boldsymbol{\alpha}_i^l$ $(i = 1, \ldots, m)$.
Output: The coefficients $\hat{\boldsymbol{\alpha}}_i$.

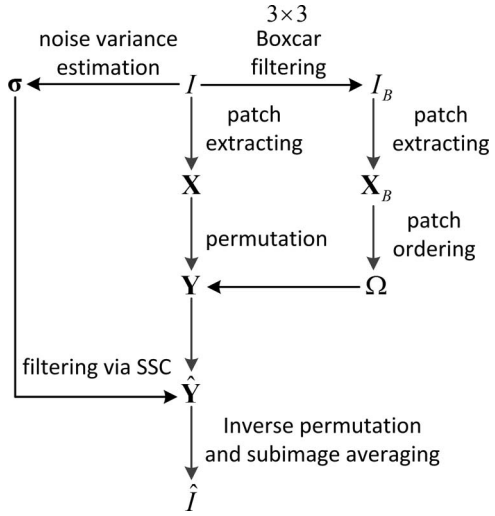

Fig. 2. Flowchart of the proposed algorithm.

TABLE I
PARAMETERS USED IN THE PROPOSED ALGORITHM

B_1	B_2	λ	n	SL	R	K	$\mathbf{D}$	$N^{(G)}$	γ
5	5	5	8	2	17	256	DCT	8	1

IV. ALGORITHM AND PARAMETER SELECTION

In this paper, we propose a new POLSAR image filtering method based on patch ordering and SSC. First, the noise variance is estimated. Then, we extract the sliding patches and order them. The ordered patches are filtered by SSC. Then, the final filtering result can be reconstructed from the filtered patches via inverse permutation and subimage averaging [22]. The proposed method is hierarchically illustrated in Fig. 2 and summarized in Algorithm 3. Table I lists the parameters used in this algorithm. These parameters have been tested and found effective over a variety of simulated and real POLSAR images and will be fixed for performance evaluation in Section V.

Algorithm 3 The proposed algorithm for POLSAR image filtering.

Input: The input POLSAR image I, the ENL L.
Noise variance estimation:
Detect strong points of I by (13) and obtain the new image I' by setting the values of strong points to zeros.
Apply a $B_1 \times B_1$ boxcar filter to I' to estimate $\mathbf{\Sigma}$.
Estimate the noise variance using (11) and (12), and then compute the noise standard deviation.
Patch extracting:
Apply a 3×3 boxcar filter to I and obtain the filtering result I_B.
Extract the sliding patches $\mathbf{X}$ and $\mathbf{X}_B$ of size $n \times n$ from I and I_B, respectively.
Patch ordering:
Order the patches $\mathbf{X}_B$ by Algorithm 1, and obtain the set Ω.
Perform permutation on $\mathbf{X}$ with the order Ω, and get the ordered patches $\mathbf{Y}$.

TABLE II
VALUES OF λ FOR DIFFERENT L AND P_{fa}

P_{fa}	$L=1$	$L=2$	$L=3$	$L=4$	$L=5$	$L=6$
10^{-5}	7.23	4.21	3.25	3.07	2.65	2.41
10^{-4}	5.83	3.70	2.88	2.60	2.34	2.20
10^{-3}	4.48	2.99	2.51	2.23	2.06	1.94
10^{-2}	3.26	2.35	2.03	1.87	1.75	1.67

Filtering via SSC:
Use $N^{(G)}$ neighboring patches of $\mathbf{Y}$ to form a group.
Perform SSC on each group. The SSC problem (29) is solved by Algorithm 2.
Obtain the filtered patches $\hat{\mathbf{Y}}$.
Inverse permutation:
Perform inverse permutation on $\hat{\mathbf{Y}}$ and obtain the patches $\hat{\mathbf{X}}$
Subimage averaging:
Reconstruct the final filtering result $\hat{I}$ from $\hat{\mathbf{X}}$ by subimage averaging [22].
Output: The final filtering result $\hat{I}$.

In the stage of noise variance estimation, there are three parameters to be set, the size of the boxcar filter B_1, the size of the median filter B_2, and the threshold λ. The size of the filter should not be too large since it may lead to big biases in noise variance estimation. In this paper, we assume that most of the areas in 5×5 windows can be regarded as homogenous areas. This assumption is also consistent with the size of the boxcar filter used in POLSAR image filtering [12], [23], [33]. Thus, we set $B_1 = 5$ and $B_2 = 5$. The threshold λ is used to detect strong isolated points. The selection of λ is related to the ENL of the noisy image and the corresponding application. Table II provides the relationship between λ, L, and the false alarm probability (P_{fa}). From (13), we can find that it is very difficult to get this relationship in theory. Thus, we just use the Monte Carlo simulation method [23] to obtain the relationship in Table II. When $L \geq 2$, the false alarm probability can reach 10^{-5} if we set $\lambda \geq 4.21$. In the case of $L = 1$ and $P_{\text{fa}} = 10^{-5}$, λ should be 7.23. If weak points should also be preserved, then the false alarm probability can be set to be 10^{-3} or 10^{-2}. The corresponding λ can be set to be around 3. In this paper, we simply set $\lambda = 5$ which can ensure that $P_{\text{fa}} < 10^{-3}$ when $L = 1$ and $P_{\text{fa}} < 10^{-5}$ when $L \geq 2$.

In [16], Elad and Aharon suggested to adopt 8×8 patches when using sparse representation to denoise images. Moreover, from (19), we can find that 8×8 patches can ensure the accuracy of the similarity of two patches and thus ensure the accuracy of patch ordering. If the ENL is small, one can choose bigger patches, such as 10×10 or 12×12. However, big patches will significantly increase the computing time of SSC. Thus, here, we select 8×8 patches, i.e., $n = 8$. From (18), we have

$$N^{(p)}\Big|_{SL=2} \approx \frac{1}{4} N^{(p)}\Big|_{SL=1}. \tag{30}$$

The computing time of the proposed method is proportional to the number of image patches. Thus, when $SL = 2$, the computing time is only a quarter of the computing time when

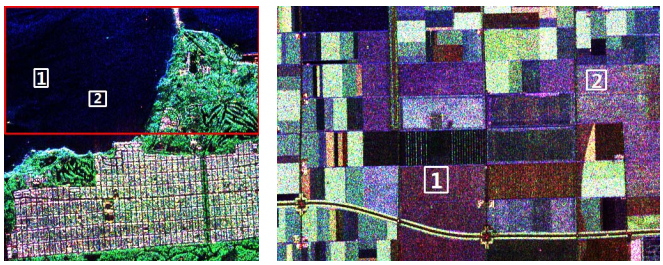

(a) (b)

Fig. 3. Test POLSAR images displayed with Pauli decomposition coefficients. The pixels in the white box are used for ENL estimation. (a) San Francisco (400×400), $L = 2.91$. The pixels in the red box are used to analyze the ratio image. (b) Flevoland (400×600), $L = 2.97$. The whole image is used to analyze the ratio image.

$SL = 1$. In Section VI, we will verify this point with real data. Moreover, we will also show that the influence on the filtering performance is very small if $SL = 2$. Thus, the sliding step SL is set to be 2. In Algorithm 1, the search range R is 17, which is the same as that in [21]. In the SSC stage, we employ the overcomplete DCT dictionary [16] of size 64×256 and use eight patches to form a group. Thus, $K = 256$, and $N^{(G)} = 8$. It should be noted that the learned dictionary will be more suitable for SSC. However, dictionary learning in the context of nonuniform noise is still a challenging problem. Thus, in this paper, we simply adopt the DCT dictionary. The parameter γ is very important and determines the balance between detail preservation and speckle removal. When γ is large, the speckle reduction ability is strong while the detail preserving ability is weak. The selection of γ depends on the size of the patches and the probability density function (pdf) of the additive noise. However, it is very hard to set γ theoretically since the pdf of the additive noise in POLSAR imagery is very complex. We find that $\gamma = 1$ is a simple but effective choice in the experiments.

V. Experimental Results

In this section, both simulated and real POLSAR images are used to demonstrate the effectiveness of the proposed method. The simulated image is generated by the Monte Carlo simulation method proposed by Lee *et al.* [23], [32]. Thus, the simulated speckle is fully developed and follows the complex Wishart distribution. We also use two four-look AIRSAR images to test the filtering performance of the proposed method for real POLSAR data. The first image [see Fig. 3(a)] is taken over San Francisco in America, and a region of 400×400 pixels is selected. The second image [see Fig. 3(b)] is taken over Flevoland in the Netherlands, and a region of 400×600 pixels is selected.

The proposed method is compared with other four filtering methods, including the refined Lee filter [2], IDAN [3], NLM-pretest [12], and NLSAR [11]. The refined Lee filter uses a 7×7 edge-aligned window, and the IDAN filter adopts an adaptive neighborhood of maximum size of 50. The free parameters used in NLM-pretest and NLSAR are the same as suggested in [11] and [12], respectively. The free parameters used in the proposed method are listed in Table I. Experimental results of the refined Lee filter and IDAN filter are obtained by the PolSARpro toolbox [33]. The implementation code of the proposed method is available in [34]. In Fig. 3, the pixels in the white box are used for ENL estimation. The ENL estimation results for the test POLSAR images are 2.91, and 2.97, respectively. The estimated ENL is used as an input parameter of the filtering methods.

A. Results With Simulated Images

In this section, we conduct a Monte Carlo experiment where samples of the simulated image are generated from the real POLSAR image Flevoland [see Fig. 3(b)]. We first select seven different homogeneous regions from the real POLSAR image Flevoland. For each region, we use the ensemble average to estimate the covariance matrix. Thus, we can get seven covariance matrices which stand for these regions. Fig. 4(a) shows a segmented image of size 493×493. This image also has seven classes which correspond to the covariance matrices obtained from Flevoland. For each pixel in Fig. 4(a), we use the corresponding covariance matrix to simulate the noisy pixel by the Monte Carlo simulation method in [23]. Fig. 4(b) presents the simulated noisy image with $L = 2$. The simulated two-look speckle which corresponds to Fig. 4(b) is shown in Fig. 5. In Fig. 4(a), the region in the white box is used for ENL estimation.

Like that in [35], we also use radiometric parameters, complex correlation parameters, and incoherent decomposition parameters $(H/A/\alpha)$ to evaluate the filtering performance for simulated images. Radiometric parameters correspond to the diagonal terms of the covariance matrix, i.e., $\mathbf{C}_{11}$, $\mathbf{C}_{22}$, and $\mathbf{C}_{33}$. Complex correlation parameters correspond to the off-diagonal terms of the covariance matrix, i.e., $\mathbf{C}_{12}$, $\mathbf{C}_{13}$, and $\mathbf{C}_{23}$. The amplitudes and the phases of the complex correlation parameters will be evaluated separatively. Here, we simply let μ, ρ, and φ denote the radiometric parameters, the amplitudes, and the phases of the complex correlation parameters, respectively. Incoherent decomposition parameters $(H/A/\alpha)$ stand for the polarimetric entropy (H), the anisotropy (A), and the mean alpha angle (α).

Then, we also use the indicator absolute relative bias which is proposed in [35] to evaluate the filtering performance for simulated images. For a given filter f and parameter θ, the estimated value $\hat{\theta}$ is obtained as the mean value from the pixels for every scattering class l. The absolute relative bias [35] of $\hat{\theta}$ is

$$\Delta_{\theta,f} = \underset{l}{\text{median}} \left\{ \left| \frac{\theta_l - \hat{\theta}_l}{\theta_l} \right| \right\} \tag{31}$$

where "median" stands for the median operator and "$|\cdot|$" is the absolute value function. In the case of μ, ρ, and φ, an additional median operator [35] is applied to reduce the number of parameters. Table III reports the filtering results of simulated data. For the radiometric parameter μ, NLSAR outperforms other methods with an absolute relative bias of only 0.005. For complex correlation parameters, the proposed method and NLSAR outperform other methods. For incoherent decomposition parameters, NLM-pretest, NLSAR, and the proposed

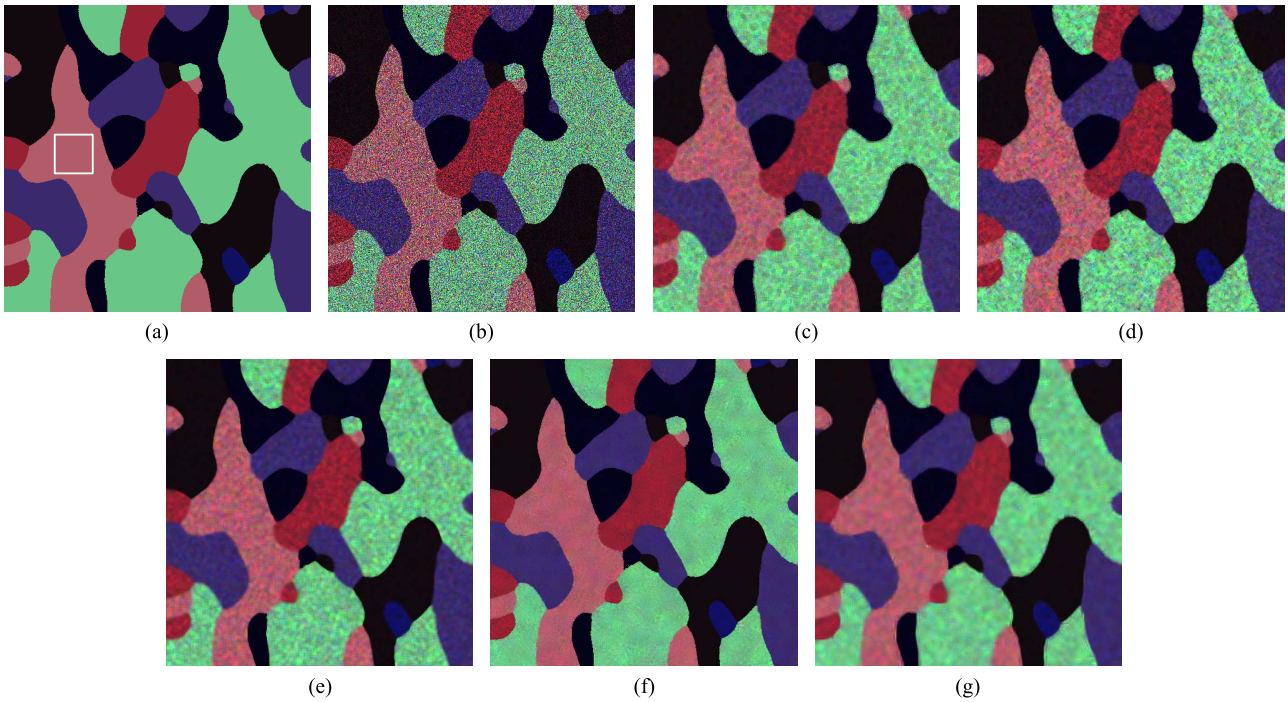

Fig. 4. Filtered images of the two-look simulated image displayed with Pauli decomposition coefficients. (a) Original image. The pixels in the white box are used for ENL estimation. (b) Noisy image. (c) Refined Lee filter. (d) IDAN. (e) NLM-pretest. (f) NLSAR. (g) Proposed.

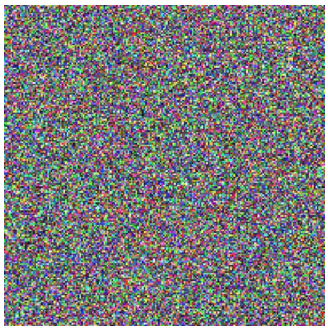

Fig. 5. Simulated two-look speckle.

TABLE III
FILTERING RESULTS FOR SIMULATED DATA. ALL MEASURES, BUT ENL, ARE ABSOLUTE RELATIVE BIASES. THE BEST RESULTS ARE EMPHASIZED IN BOLDFACE

	μ	ρ	φ	H	A	α	ENL
Refined Lee	0.078	0.226	0.214	0.017	0.030	0.033	57.84
IDAN	0.144	0.231	0.082	0.017	0.086	**0.006**	61.48
NLM-Pretest	0.016	0.138	0.087	0.011	0.015	0.012	93.57
NLSAR	**0.005**	0.139	**0.033**	**0.008**	**0.010**	**0.006**	196.24
Proposed	0.042	**0.060**	0.052	0.013	0.025	0.014	**209.60**

method achieve very good performance with absolute relative biases around 0.01. Table III also presents the ENL [25], [35] results which indicate the speckle reduction ability in homogeneous areas. Larger ENL corresponds to stronger speckle reduction ability. Thus, we can find that the proposed method and NLSAR have stronger speckle reduction ability that other methods.

Fig. 4 shows the filtered images displayed with Pauli decomposition coefficients. We can find that NLSAR achieves very impressive filtering performance in both speckle reduction and detail preserving. The proposed method also has very strong speckle reduction ability; however, it blurs the edges a little. The other three methods also blur the details. To focus on the edge preserving ability, we apply the Canny detector [36] to the HH polarization channel of the original and filtered images in Fig. 4, and the results are given in Fig. 6. The performance of the Canny detector depends on the setting of its parameters. As suggested in [37], we set the parameters of the Canny detector that provide the best performance for each filtered image. In Fig. 6, we provide the standard deviation (σ_g) of the Gaussian filter used in the Canny detector for each filtered image. The other parameters in the Canny detector are the same for all the filtered images. The refined Lee filter and NLM-pretest filter introduce some false edges in flat areas. The IDAN filter and proposed method only produce few false edges in flat areas and remove few details. Fig. 6(f) is the closest to Fig. 6(a). Thus, in Fig. 6, NLSAR has the best edge preserving ability.

From Fig. 4, Fig. 6, and Table III, we can conclude that NLSAR achieves very good filtering performance and the proposed method also provides very competitive results. In this section, the simulated image only consists of several homogenous regions, and the simulated speckle is white. However, in real POLSAR images, the speckle is correlated and may not be fully developed. Thus, we will focus on real POLSAR image despeckling in Section V-B.

B. Results With Real POLSAR Images

Fig. 7 shows the filtered images of San Francisco displayed with Pauli decomposition coefficients. The refined Lee filter blurs the edges in the urban region and introduces artifacts around the edges. The IDAN filter and the NLM-pretest filter also remove some details in the urban region. The proposed method and NLSAR outperform the other methods in urban

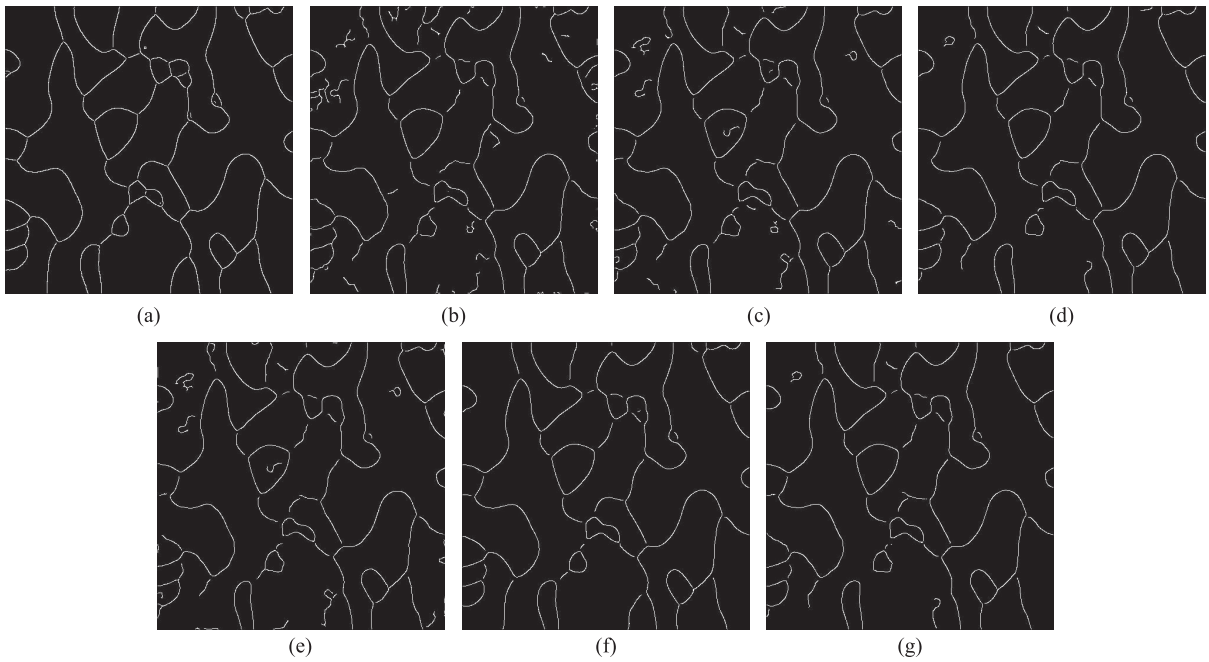

Fig. 6. Edges detected by the Canny method applied to the HH polarization channel of the original and filtered images. (a) Original image, $\sigma_g = 1.41$. (b) Noisy image, $\sigma_g = 4.53$. (c) Refined Lee filter, $\sigma_g = 4.24$. (d) IDAN, $\sigma_g = 4.24$. (e) NLM-pretest, $\sigma_g = 4.24$. (f) NLSAR, $\sigma_g = 3.82$. (g) Proposed, $\sigma_g = 3.82$.

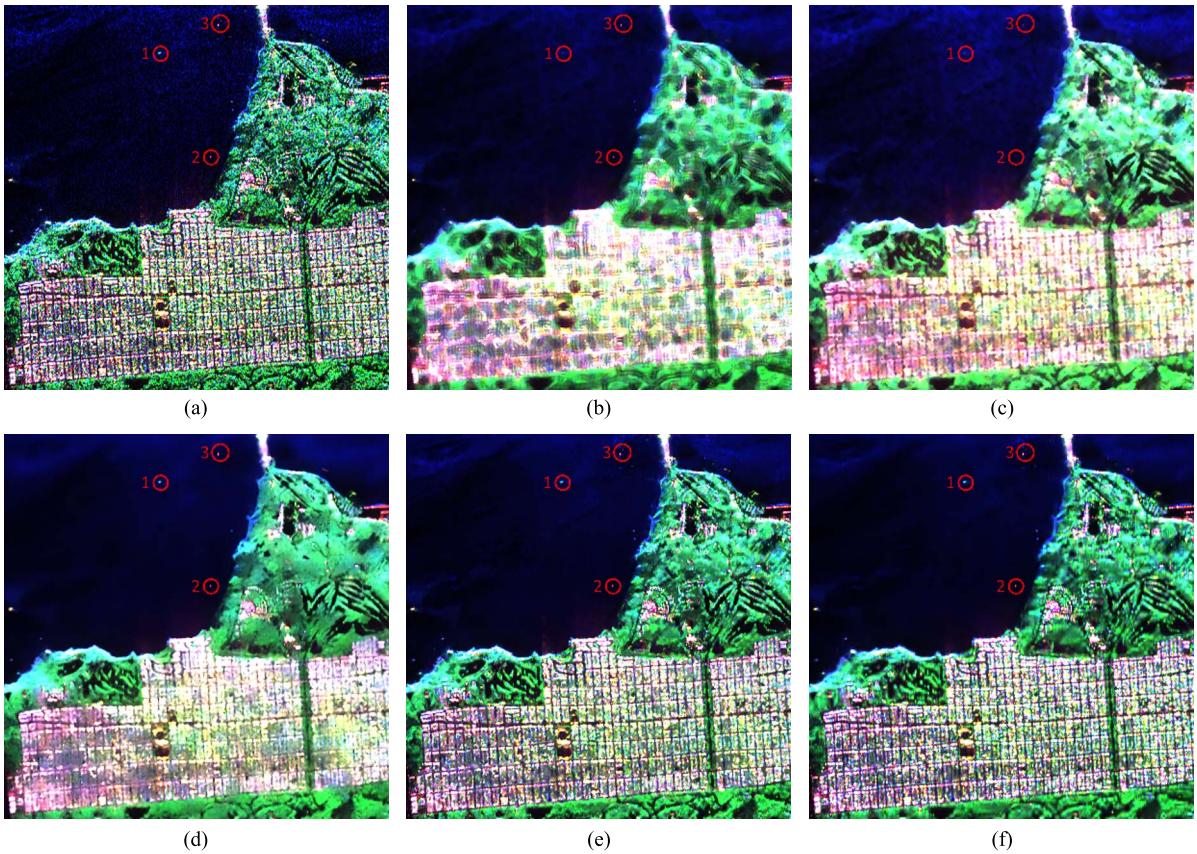

Fig. 7. Filtered images of San Francisco displayed with Pauli decomposition coefficients. (a) Original image. (b) Refined Lee filter. (c) IDAN. (d) NLM-pretest. (e) NLSAR. (f) Proposed.

areas. In Fig. 7(a), we select three regions which are marked by red circles to analyze the point target preserving ability. The point in region 1 is preserved well by NLM-pretest, NLSAR, and the proposed method but is blurred by the other methods. The point in region 2 can be easily found in Fig. 7(b)–(f). There are two points in region 3. One is strong, and the other is weak.

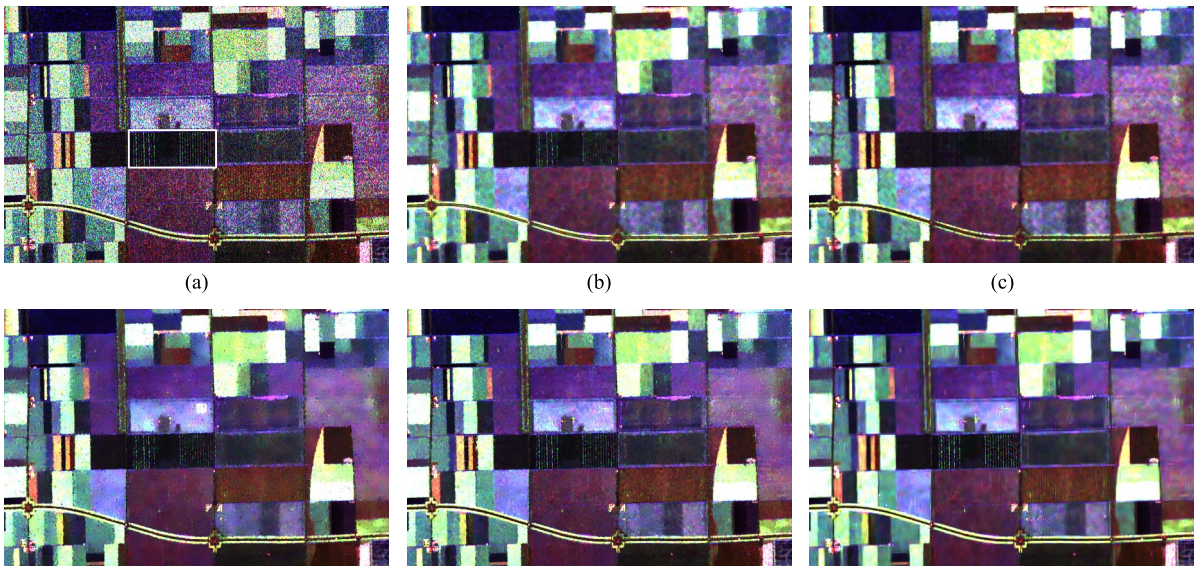

Fig. 8. Filtered images of Flevoland displayed with Pauli decomposition coefficients. The filtered images of the region in the white box are shown in Fig. 9. (a) Original image. (b) Refined Lee filter. (c) IDAN. (d) NLM-pretest. (e) NLSAR. (f) Proposed.

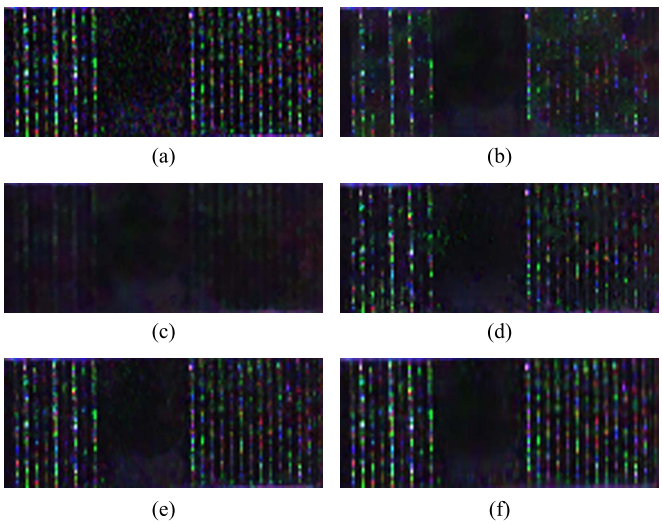

Fig. 9. Filtered images of the region in the white box in Fig. 8(a). (a) Original image. (b) Refined Lee filter. (c) IDAN. (d) NLM-pretest. (e) NLSAR. (f) Proposed.

The strong point can be easily found in Fig. 7(b)–(f). However, the weak point is only preserved by NLSAR and the proposed method. Thus, the proposed method and NLSAR have very strong point target preserving ability.

Fig. 8 shows the filtered images of Flevoland displayed with Pauli decomposition coefficients. In Fig. 8, we can also find that the proposed method has very strong detail preserving ability from the road and the edges of the farmland. Let us focus on the region in the white box in Fig. 8(a). Filtered images of this region are shown in Fig. 9. Almost all the details are blurred by IDAN. The refined Lee filter also blurs a lot of details. The NLM-pretest filter removes a few details. The proposed method and NLSAR outperform the other methods and preserve almost all the details.

TABLE IV
ENL OF FILTERED IMAGES. THE BEST RESULTS ARE EMPHASIZED IN BOLDFACE

	San Francisco		Flevoland	
	Region 1	Region 2	Region 1	Region 2
Noisy	2.91	2.90	2.96	2.97
Refined Lee	58.32	50.57	42.67	49.21
IDAN	51.59	55.44	55.58	58.33
NLM-Pretest	**269.65**	**258.27**	34.00	79.60
NLSAR	100.00	100.87	47.53	58.81
Proposed	172.47	150.39	**87.30**	**126.31**

TABLE V
MEAN AND VARIANCE OF RATIO IMAGES. THE BEST RESULTS ARE EMPHASIZED IN BOLDFACE

	San Francisco					
	$E[r_{hh}]$	$E[r_{hv}]$	$E[r_{vv}]$	var $[r_{hh}]$	var $[r_{hv}]$	var $[r_{vv}]$
Refined Lee	1.184	1.133	1.178	0.617	0.556	0.588
IDAN	1.256	1.221	1.244	1.188	0.849	0.903
NLM-Pretest	0.972	0.972	0.973	0.387	**0.339**	0.379
NLSAR	0.953	0.959	0.952	0.198	0.174	0.198
Proposed	**1.012**	**1.010**	**1.012**	**0.328**	0.275	**0.319**
	Flevoland					
	$E[r_{hh}]$	$E[r_{hv}]$	$E[r_{vv}]$	var $[r_{hh}]$	var $[r_{hv}]$	var $[r_{vv}]$
Refined Lee	1.118	1.072	1.115	0.393	0.429	0.377
IDAN	1.159	1.175	1.154	0.662	0.735	0.578
NLM-Pretest	0.974	0.968	0.976	0.263	0.269	0.256
NLSAR	0.955	0.952	0.955	0.174	0.176	0.172
Proposed	**1.011**	**1.015**	**1.011**	**0.301**	**0.326**	**0.293**

Here, we also use the ENL to evaluate the speckle reduction ability in homogeneous areas. Table IV gives the ENL results for San Francisco and Flevoland using different filtering methods. For each image, two homogeneous regions (see Fig. 3) are selected to estimate the ENL. We can find that the proposed method and NLM-pretest filter have much stronger speckle reduction ability than the other methods. In Fig. 8(d) and (e),

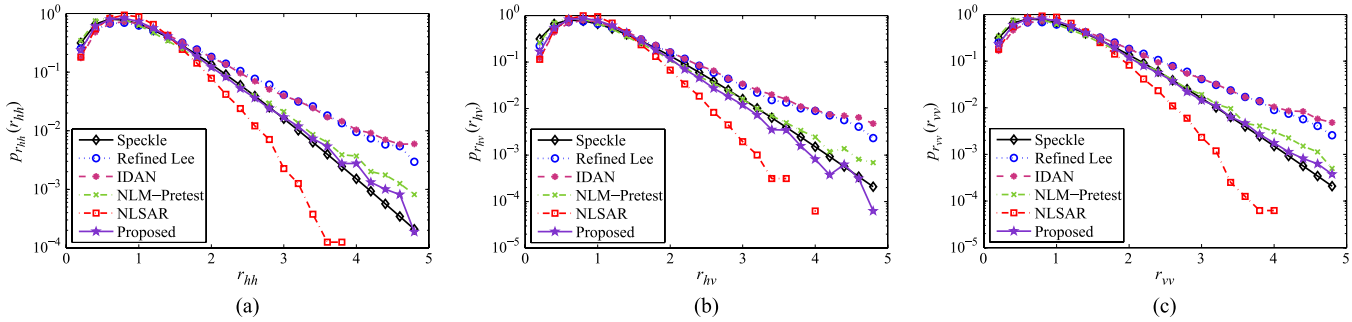

Fig. 10. PDFs of ratio images for San Francisco. The pdf of the actual speckle is used as a reference. "◊": Actual speckle. "○": Refined Lee filter. "•": IDAN. "×": NLM-pretest. "□": NLSAR. "⋆": Proposed method. (a) r_{hh}. (b) r_{hv}. (c) r_{vv}.

the ENL results are not as good as in Fig. 7(d) and (e) since NLM-pretest and NLSAR produce some artifacts in flat areas.

Another indicator to evaluate the filtering results is the ratio image which is widely used in SAR image despeckling [38], [39]. The ratio image is the pointwise ratio between the original image and filtered image. For example, the ratio image of the HH channel is

$$r_{\mathrm{hh}} = \frac{\mathbf{C}_{11}}{\hat{\mathbf{\Sigma}}_{11}} \tag{32}$$

where $\hat{\mathbf{\Sigma}}$ is the filtered image. The ratio image stands for the noise removed by image filtering, and the best result corresponds to the ratio image which is the closest to the actual speckle. Thus, we should select the regions where the speckle is fully developed to analyze the ratio image. In general, the speckle in flat areas such as the grass, short vegetation, and calm sea with low waves [40] is well developed. In Fig. 3(a), the pixels in the red box which correspond to the sea and grass are selected. In Fig. 3(b), the whole image is used to analyze the ratio image since it is acquired over the farmlands in Flevoland.

Then, the ratio image is analyzed by its mean, variance, and pdf. The mean and variance of the ratio image indicate the bias and speckle power suppression [41], respectively. A mean value of the ratio image close to 1 indicates an unbiased estimation. Measured ENL results on the original images are 2.91 for San Francisco and 2.97 for Flevoland, respectively. Thus, the variances of the actual speckle are 0.344 and 0.337 for San Francisco and Flevoland, respectively. The pdf of the ratio image can evaluate the similarity of the actual speckle and ratio image.

Table V reports the results of ratio images for San Francisco and Flevoland, and the best results are shown in boldface. The results of different channels are quite consistent. From the results of $E[r_{hh}]$, $E[r_{hv}]$, and $E[r_{vv}]$, we can find that the proposed method has the smallest bias. From the results of $\mathrm{var}[r_{hh}]$, $\mathrm{var}[r_{hv}]$, and $\mathrm{var}[r_{vv}]$, we can conclude that the proposed method outperforms the other methods and has very good speckle power suppression. Fig. 10 presents the pdfs of ratio images for San Francisco with logarithmic scale for the y-axis. The speckle of each channel follows the Gamma distribution, and the tailing part of the pdf seems like a straight line. The results of different channels are also very consistent, indicating that the ratio images obtained by the proposed method are the closest to the actual speckle. Thus, from the view of the ratio image, the proposed method performs better than the other methods.

Here, we would like to discuss why the proposed method can achieve such performance when handling the homogeneous and heterogeneous regions. For homogeneous regions such as the sea in Fig. 7 and the farmland in Fig. 8, the speckle is well developed and follows the complex Wishart distribution. Thus, the noise variance is well estimated by (11) and (12) when dealing with homogeneous regions. The homogeneous regions are well filtered by SSC, and thus, the proposed method has very strong speckle reduction ability in homogeneous areas. For heterogeneous regions such as the urban region in Fig. 7, the speckle is not well developed, and the noise variance is underestimated by (11) and (12). The depth of filtering is relatively low in heterogeneous regions, and thus, the proposed method has very good detail preserving ability.

C. Effect on the Scattering Characteristics

Here, we use H/α decomposition [42] which extracts the polarimetric entropy (H) and averaged alpha angle (α) from the coherency matrix to analyze the effect on the scattering characteristics. Fig. 11 shows the entropy values of filtered images for San Francisco. In Fig. 11(a), the entropy obtained from the original image is relatively low because of insufficient averaging. In Fig. 11(b), we can find that the resolution decreases, particularly in the city area. The entropy image of IDAN [see Fig. 11(c)] loses some details in the city and grass areas. In the entropy images of NLM-pretest [see Fig. 11(d)], NLSAR [see Fig. 11(e)], and the proposed method [see Fig. 11(f)], the entropy is relatively low in the sea, and the entropy between the sea and land can be easily distinguished. However, for the city and grass areas which consist of complicated scattering mechanisms, the proposed method and NLSAR outperform other methods since both methods preserve most of the scattering mechanisms.

To further evaluate the effect on the scattering characteristics, three regions shown in Fig. 11(a) are selected to plot the H/α parameters. The first region is the ocean area which corresponds to low entropy surface scatter. The second region is the city area which has complicated scattering mechanisms. The third region is the grass area which corresponds to high entropy. The scatters of the original image [see Fig. 12(a)] disperse on

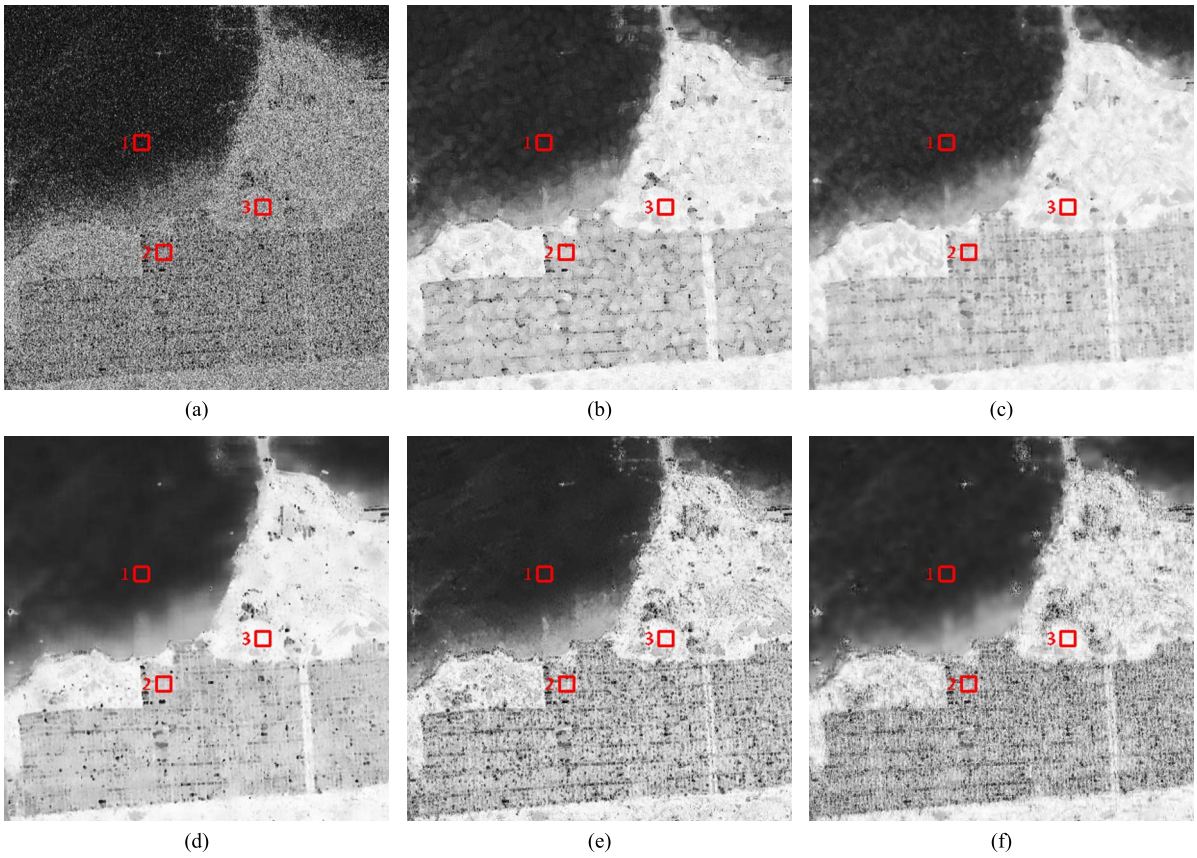

Fig. 11. Entropy values of filtered images for San Francisco. Three regions shown in (a) are selected to plot the H/α parameters in Fig. 12. (a) Original image. (b) Refined Lee filter. (c) IDAN. (d) NLM-pretest. (e) NLSAR. (f) Proposed.

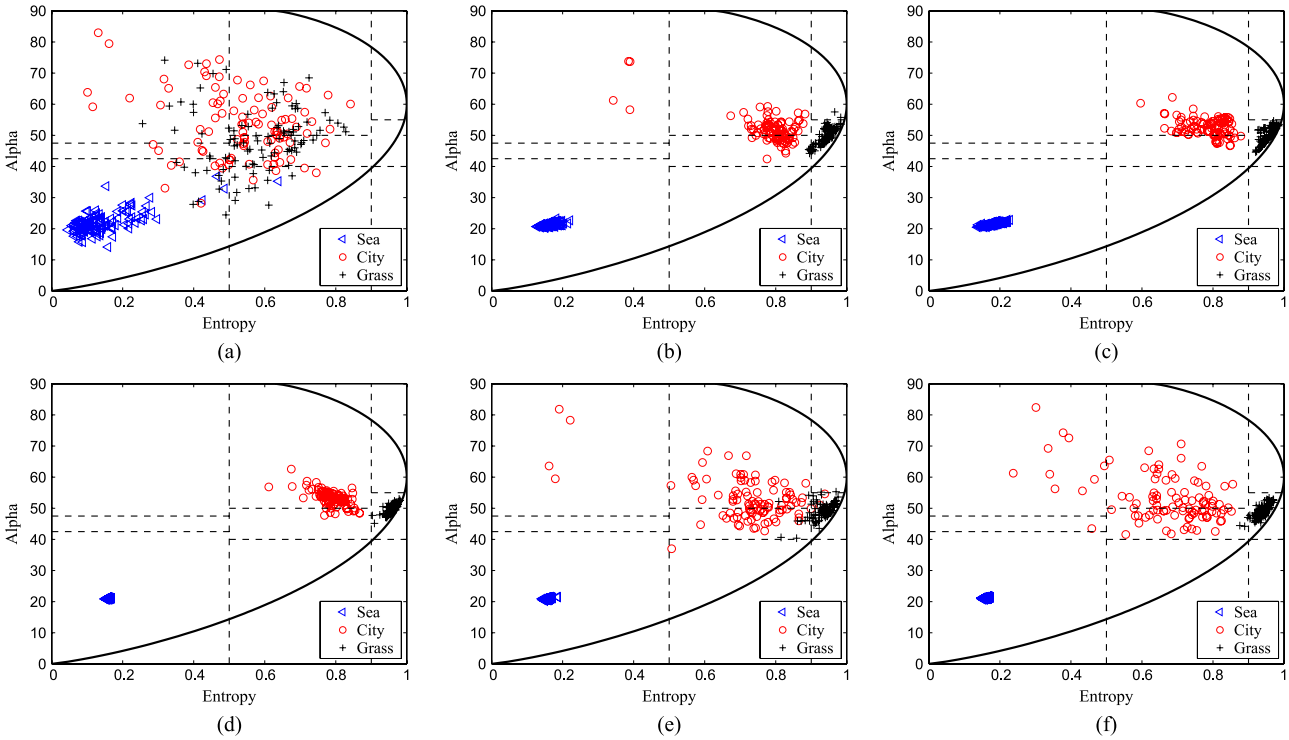

Fig. 12. Scatterplot in the H/α plane of samples from the filtered images for San Francisco. "◁": Sea. "○": City. "+": Grass. (a) Original image. (b) Refined Lee filter. (c) IDAN. (d) NLM-pretest. (e) NLSAR. (f) Proposed.

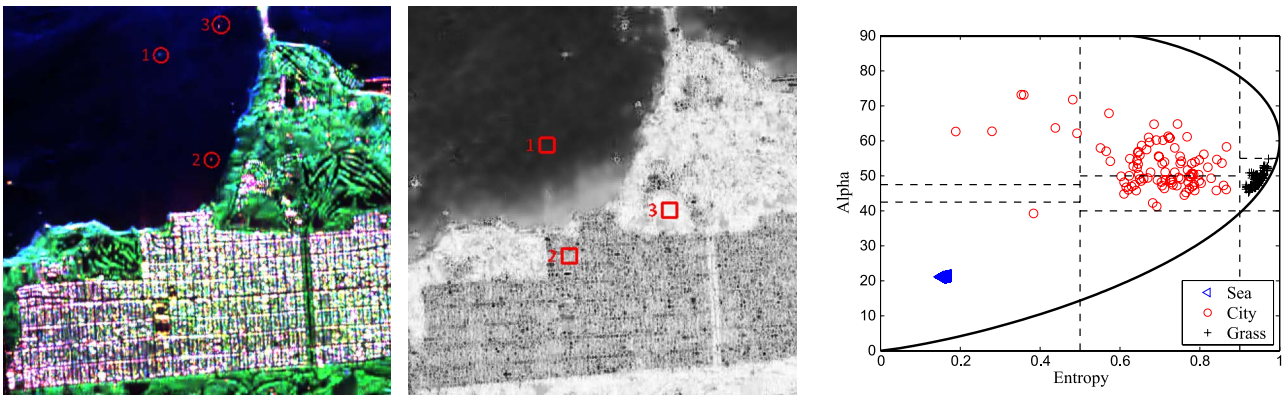

(a) (b) (c)

Fig. 13. Filtered results of San Francisco by the proposed method without strong isolated point detection. (a) Filtered image displayed with Pauli decomposition coefficients. (b) Entropy. (c) Scatterplot in the H/α plane.

the H/α plane. The scatters of different terrains can be distinguished after filtering. For the ocean area, the proposed method and NLM-pretest perform better than other filters because the scatters of the ocean area intensively converge. For the city area, the scatters in the proposed method and NLSAR are more random than in the other filters because the proposed method and NLSAR retain the complicated scattering mechanisms in the city area. For the grass area, most of the scatters lie in the zone of high entropy.

TABLE VI
RESULTS OF THE ABSOLUTE RELATIVE BIASES FOR DIFFERENT PARAMETERS. FOR EACH CASE, THE CHANGED PARAMETER IS EMPHASIZED IN BOLDFACE

No.	B_1	n	SL	μ	ρ	φ	H	A	α
1	5	8	2	0.042	0.060	0.052	0.013	0.025	0.014
2	**3**	8	2	0.109	0.116	0.055	0.016	0.046	0.017
3	**7**	8	2	0.031	0.057	0.069	0.012	0.018	0.012
4	5	8	**1**	0.041	0.057	0.049	0.012	0.022	0.013
5	5	8	**3**	0.042	0.058	0.060	0.012	0.028	0.014
6	5	**12**	2	0.051	0.079	0.057	0.017	0.023	0.014

VI. DISCUSSION

In this section, we will discuss the effects of strong point detection and several parameters. Moreover, the time consumption of the proposed method will also be discussed.

A. Effect of Strong Point Detection

In Section V-B, we have shown that the proposed method has very strong point target preserving ability. Here, we ascribe the strong point target preserving ability to the point detection in the noise variance estimation since the noise variance around strong points is underestimated. Fig. 13(a) presents the filtered image of San Francisco by the proposed method without strong isolated point detection. It can be found that the point in region 1 is blurred without strong isolated point detection. A similar phenomenon can also be found from other points. Thus, strong isolated point detection is an important step in the proposed method.

Although strong point detection can help to preserve strong point targets, it will also reduce the speckle filtering power in the neighborhood of strong targets. Thus, this step will have a relevant effect in urban areas where many isolated bright targets can appear due to the presence of trihedral structures. By comparing Fig. 13(a) with Fig. 7(f), we can find that the step of strong point detection reduces the speckle filtering power a little in urban areas. In Fig. 13, we also provide the entropy and scatterplot results obtained by the proposed method without strong isolated point detection. In Fig. 13(b), we can see that the point targets are a little blurred. However, the entropy result around the point targets is better than that in Fig. 11(f). In Fig. 13(c), the scatters in the urban area are not so disperse like that in Fig. 12(f). Thus, it is an important topic to reduce the influence of strong point detection, particularly in urban areas, and we will focus on this problem in our future work.

B. Discussion on Parameter Tuning

In this section, we mainly use the simulated image to discuss the influences of three parameters, B_1, n, and SL. The indicators used in Section V-A are also adopted here. Table VI reports the results of the absolute relative biases for different parameters. Other free parameters are the same as in Table I.

We can find that the absolute relative biases of μ, ρ, and A are relatively large when $B_1 = 3$. The simulated image [see Fig. 4(b)] is composed of homogenous areas. Thus, the results are better when $B_1 = 7$. However, the filtering performance improves only a little when $B_1 = 7$. Thus, in this paper, we just set $B_1 = 5$. In Table VI, one can see that the differences between the first row $(SL = 2)$, the fourth row $(SL = 1)$, and the fifth row $(SL = 3)$ are very small. Thus, the influence on the filtering performance is very small when $SL = 2$, and it is reasonable to set SL to be 2. When $n = 12$, the absolute relative biases of incoherent decomposition parameters change a little. However, for μ, ρ, and φ, the results of absolute relative biases increase about 0.005–0.019. Thus, we do not suggest to use patches of size 12×12 here.

TABLE VII
COMPUTING TIME OF EACH STEP FOR FLEVOLAND

Procedure	Computing time
Noise variance estimation	2.9s
Patch ordering	3.5s
SSC	39.6s
Subimage averaging	7.5s
Total	53.5s

TABLE VIII
COMPUTING TIME FOR FLEVOLAND WITH DIFFERENT PARAMETERS. OTHER PARAMETERS ARE GIVEN IN TABLE I

No.	Image size	n	SL	Computing time
1	400×600	8	2	53.5s
2	400×600	8	1	219.2s
3	400×600	12	2	368.5s
4	200×300	8	2	22.9s

C. Time Consumption

In Table VII, we report the computing time of the proposed method for Flevoland. The code [34] of the proposed method was written in C source MEX-file and run by MATLAB, and the PC used to run this code had an Intel Core i5 processor with 2.80-GHz main frequency and 8.00-GB main memory. It typically takes around 50 s for the proposed method to denoise a 400×600 POLSAR image. In addition, Table VII also gives the computing time of each step. It can be found that SSC is quite time consuming. The computing time of SSC takes about 75% of the total time. Here, we can use parallel computing to further reduce the computing time of SSC. With the help of the parallel computing technology, the time complexity of the proposed method is acceptable in polarimetric SAR applications.

As stated in Section IV, the parameters n and SL can significantly affect the computing time of the proposed method. Table VIII presents the computing time for Flevoland with different parameters. The computing time in the second condition $(SL = 1)$ is about three times larger than that in the first condition $(SL = 2)$, and this is quite consistent with (30). Thus, we can greatly reduce the computing time by setting SL to be 2. In the third row of Table VIII, the computing time increases a lot with the increase of n. Thus, from the view of time consumption, we also do not suggest to use big patches. We reduce the size of Flevoland to 200×300 by simply sampling every other pixel, and the corresponding computing time is about 23 s. In fact, the computing time of SSC is proportional to the size of the image. Thus, the computing time of the proposed method is also approximately proportional to the size of the image.

VII. CONCLUSION

In this paper, a transform-domain filtering method for POLSAR images was proposed. We developed a signal-dependent additive noise model for the full POLSAR data and extended the patch ordering algorithm based on POLSAR statistics. With the derived additive noise model, we then performed sparse reconstruction using SSC on the ordered patches. The final result was reconstructed from the filtered patches via inverse permutation and subimage averaging.

We used both simulated and real POLSAR images to validate the effectiveness of the proposed method. For simulated images, the results show that the proposed method achieves very good performance in terms of the radiometric parameters, complex correlation parameters, and incoherent decomposition parameters and has very good edge preserving ability. For real POLSAR images, we used the ENL, ratio image, and H/α decomposition to evaluate the filtering performance. The proposed method has very strong speckle reduction ability and detail preserving ability. Moreover, the corresponding ratio image is the closest to the actual speckle. The results of H/α decomposition also show that the proposed method converges the same scattering mechanism and retains the complicated scattering mechanisms effectively.

As future works, the proposed method may benefit from improved dictionary learning in the context of nonuniform noise which is still a challenging problem. In addition, we will also try to reduce the influence of strong point detection, particularly in urban areas.

APPENDIX A
DERIVATION OF THE NOISE VARIANCE

In this appendix, we derive the variances of elements in $\mathbf{Z}$. Let $\mathbf{A} = L\mathbf{C}$. As stated in [24], the characteristic function of the variables $\mathbf{A}_{11}, \ldots, \mathbf{A}_{33}, 2\mathrm{Re}(\mathbf{A}_{12}), 2\mathrm{Im}(\mathbf{A}_{12}), \ldots, 2\mathrm{Re}(\mathbf{A}_{23}), 2\mathrm{Im}(\mathbf{A}_{23})$ is

$$\begin{aligned}\Phi_{\mathbf{A}}(\mathbf{\Theta}) &= E\left[\exp\left(j\mathrm{Tr}(\mathbf{A}\mathbf{\Theta})\right)\right] \\ &= |\mathbf{\Sigma}|^{-L}|\mathbf{\Sigma}^{-1} - j\mathbf{\Theta}|^{-L} \\ &= |\mathbf{I} - j\mathbf{\Sigma}\mathbf{\Theta}|^{-L} \end{aligned} \tag{33}$$

where $E[\cdot]$ stands for the expectation operation, $\mathbf{\Theta}$ is a Hermitian matrix, and $\mathbf{I}$ is the identity matrix.

By setting

$$\mathbf{\Theta} = \begin{bmatrix} \theta & 0 & 0 \\ 0 & 0 & 0 \\ 0 & 0 & 0 \end{bmatrix} \tag{34}$$

we obtain the characteristic function of $\mathbf{A}_{11}$

$$\begin{aligned}\Phi_{\mathbf{A}_{11}}(\theta) &= E\left[\exp(j\mathbf{A}_{11}\theta)\right] \\ &= (1 - j\mathbf{\Sigma}_{11}\theta)^{-L}. \end{aligned} \tag{35}$$

Then, we can calculate the first-order and the second-order moment of $\mathbf{A}_{11}$ from (35)

$$E[\mathbf{A}_{11}] = \left[\frac{1}{j}\frac{d\Phi_{\mathbf{A}_{11}}(\theta)}{d\theta}\right]\Bigg|_{\theta=0} = L\mathbf{\Sigma}_{11} \tag{36}$$

$$E\left[\mathbf{A}_{11}^2\right] = \left[-\frac{d^2\Phi_{\mathbf{A}_{11}}(\theta)}{d\theta^2}\right]\Bigg|_{\theta=0} = (L^2 + L)\mathbf{\Sigma}_{11}^2 \tag{37}$$

respectively. Thus, the variance of $\mathbf{A}_{11}$ is

$$\mathrm{var}[\mathbf{A}_{11}] = L\mathbf{\Sigma}_{11}^2. \tag{38}$$

The variance of $\mathbf{Z}_{11}$ is

$$\begin{aligned}\mathrm{var}[\mathbf{Z}_{11}] &= \mathrm{var}[\mathbf{C}_{11}] \\ &= \frac{\mathrm{var}[\mathbf{A}_{11}]}{L^2} \\ &= \frac{\boldsymbol{\Sigma}_{11}^2}{L}. \end{aligned} \tag{39}$$

The variances of $\mathbf{Z}_{22}$ and $\mathbf{Z}_{33}$ can be calculated in the same way.

By setting

$$\boldsymbol{\Theta} = \begin{bmatrix} 0 & \frac{\theta}{2} & 0 \\ \frac{\theta}{2} & 0 & 0 \\ 0 & 0 & 0 \end{bmatrix} \tag{40}$$

we get the characteristic function of $\mathrm{Re}(\mathbf{A}_{12})$, shown in

$$\begin{aligned}\Phi_{\mathrm{Re}(\mathbf{A}_{12})}(\theta) &= E\left[\exp\left(j\mathrm{Re}(\mathbf{A}_{12})\theta\right)\right] \\ &= \left(1 + \frac{1}{4}\theta^2\boldsymbol{\Sigma}_{11}\boldsymbol{\Sigma}_{22} - \frac{1}{4}\theta^2\mathrm{Re}(\boldsymbol{\Sigma}_{12})^2 \right. \\ &\quad \left. - \frac{1}{4}\theta^2\mathrm{Im}(\boldsymbol{\Sigma}_{12})^2 - j\mathrm{Re}(\boldsymbol{\Sigma}_{12})\theta\right)^{-L}. \end{aligned} \tag{41}$$

The first-order and the second-order moment of $\mathrm{Re}(\mathbf{A}_{12})$ are

$$E[\mathrm{Re}(\mathbf{A}_{12})] = L\mathrm{Re}(\boldsymbol{\Sigma}_{12}) \tag{42}$$

$$\begin{aligned}E\left[\mathrm{Re}(\mathbf{A}_{12})^2\right] &= L^2\mathrm{Re}(\boldsymbol{\Sigma}_{12})^2 \\ &\quad + \frac{L}{2}\left[\mathrm{Re}(\boldsymbol{\Sigma}_{12})^2 - \mathrm{Im}(\boldsymbol{\Sigma}_{12})^2 + \boldsymbol{\Sigma}_{11}\boldsymbol{\Sigma}_{22}\right] \end{aligned} \tag{43}$$

respectively. Thus, the variance of $\mathrm{Re}(\mathbf{A}_{12})$ is

$$\mathrm{var}\left[\mathrm{Re}(\mathbf{A}_{12})\right] = \frac{L}{2}\left[\mathrm{Re}(\boldsymbol{\Sigma}_{12})^2 - \mathrm{Im}(\boldsymbol{\Sigma}_{12})^2 + \boldsymbol{\Sigma}_{11}\boldsymbol{\Sigma}_{22}\right]. \tag{44}$$

The variance of $\mathrm{Re}(\mathbf{Z}_{12})$ is

$$\mathrm{var}\left[\mathrm{Re}(\mathbf{Z}_{12})\right] = \frac{1}{2L}\left[\mathrm{Re}(\boldsymbol{\Sigma}_{12})^2 - \mathrm{Im}(\boldsymbol{\Sigma}_{12})^2 + \boldsymbol{\Sigma}_{11}\boldsymbol{\Sigma}_{22}\right]. \tag{45}$$

In the same way, we can also obtain the variances of $\mathrm{Re}(\mathbf{Z}_{13})$ and $\mathrm{Re}(\mathbf{Z}_{23})$.

By setting

$$\boldsymbol{\Theta} = \begin{bmatrix} 0 & \frac{j\theta}{2} & 0 \\ -j\theta/2 & 0 & 0 \\ 0 & 0 & 0 \end{bmatrix} \tag{46}$$

we obtain the characteristic function of $\mathrm{Im}(\mathbf{A}_{12})$, shown in

$$\begin{aligned}\Phi_{\mathrm{Im}(\mathbf{A}_{12})}(\theta) &= E\left[\exp\left(j\mathrm{Im}(\mathbf{A}_{12})\theta\right)\right] \\ &= \left(1 + \frac{1}{4}\theta^2\boldsymbol{\Sigma}_{11}\boldsymbol{\Sigma}_{22} - \frac{1}{4}\theta^2\mathrm{Re}(\boldsymbol{\Sigma}_{12})^2 \right. \\ &\quad \left. - \frac{1}{4}\theta^2\mathrm{Im}(\boldsymbol{\Sigma}_{12})^2 - j\mathrm{Im}(\boldsymbol{\Sigma}_{12})\theta\right)^{-L}. \end{aligned} \tag{47}$$

We can find that (47) can be obtained from (41) by replacing $\mathrm{Re}(\mathbf{A}_{12})$ with $\mathrm{Im}(\mathbf{A}_{12})$. Thus, we can immediately get the variance of $\mathrm{Im}(\mathbf{Z}_{12})$

$$\mathrm{var}\left[\mathrm{Im}(\mathbf{Z}_{12})\right] = \frac{1}{2L}\left[\mathrm{Im}(\boldsymbol{\Sigma}_{12})^2 - \mathrm{Re}(\boldsymbol{\Sigma}_{12})^2 + \boldsymbol{\Sigma}_{11}\boldsymbol{\Sigma}_{22}\right]. \tag{48}$$

Then, we can obtain similar results of $\mathrm{Im}(\mathbf{Z}_{13})$ and $\mathrm{Im}(\mathbf{Z}_{23})$ in the same way.

ACKNOWLEDGMENT

The authors would like to thank Dr. J. Chen for providing the NLM-pretest code and Dr. C. Deledalle for providing the NLSAR code. The authors would also like to thank the European Space Agency for the free use of PolSARpro and the reviewers for their helpful comments.

REFERENCES

[1] J. S. Lee, M. R. Grunes, and S. A. Mango, "Speckle reduction in multipolarization, multifrequency SAR imagery," *IEEE Trans. Geosci. Remote Sens.*, vol. 29, no. 4, pp. 535–544, Jul. 1991.

[2] J. S. Lee, M. R. Grunes, and G. De Grandi, "Polarimetric SAR speckle filtering and its implication for classification," *IEEE Trans. Geosci. Remote Sens.*, vol. 37, no. 5, pp. 2363–2373, Sep. 1999.

[3] G. Vasile, E. Trouvé, J. S. Lee, and V. Buzuloiu, "Intensity-driven adaptive neighborhood technique for polarimetric and interferometric SAR parameters estimation," *IEEE Trans. Geosci. Remote Sens.*, vol. 44, no. 6, pp. 1609–1621, Jun. 2006.

[4] J. S. Lee, M. R. Grunes, D. L. Schuler, E. Pottier, and L. Ferro-Famil, "Scattering-model-based speckle filtering of polarimetric SAR data," *IEEE Trans. Geosci. Remote Sens.*, vol. 44, no. 1, pp. 176–187, Jan. 2006.

[5] C. López-Martínez and X. Fàbregas, "Model-based polarimetric SAR speckle filter," *IEEE Trans. Geosci. Remote Sens.*, vol. 46, no. 11, pp. 3894–3907, Nov. 2008.

[6] C. López-Martínez and X. Fàbregas, "Polarimetric SAR speckle noise model," *IEEE Trans. Geosci. Remote Sens.*, vol. 41, no. 10, pp. 2232–2242, Oct. 2003.

[7] J. Gu *et al.*, "Speckle filtering in polarimetric SAR data based on the subspace decomposition," *IEEE Trans. Geosci. Remote Sens.*, vol. 42, no. 8, pp. 1635–1641, Aug. 2004.

[8] S. Foucher, G. Farage, and G. Benie, "Polarimetric SAR image filtering with trace-based partial differential equations," *Can. J. Remote Sens.*, vol. 33, no. 3, pp. 226–236, Jan. 2007.

[9] A. Buades, B. Coll, and J. M. Morel, "A review of image denoising algorithms, with a new one," *Multisc. Model. Simul.*, vol. 4, no. 2, pp. 490–530, Jul. 2005.

[10] C. Deledalle, L. Denis, and F. Tupin, "Iterative weighted maximum likelihood denoising with probabilistic patch-based weights," *IEEE Trans. Image Process.*, vol. 18, no. 12, pp. 2661–2672, Dec. 2009.

[11] C. Deledalle, L. Denis, F. Tupin, A. Reigber, and M. Jäger, "NL-SAR: A unified nonlocal framework for resolution-preserving (Pol)(In) SAR denoising," *IEEE Trans. Geosci. Remote Sens.*, vol. 53, no. 4, pp. 2021–2038, Apr. 2015.

[12] J. Chen, Y. Chen, W. An, Y. Cui, and J. Yang, "Nonlocal filtering for polarimetric SAR data: A pretest approach," *IEEE Trans. Geosci. Remote Sens.*, vol. 49, no. 5, pp. 1744–1754, May 2011.

[13] K. Conradsen, A. A. Nielsen, J. Schou, and H. Skriver, "A test statistic in the complex Wishart distribution and its application to change detection in polarimetric SAR data," *IEEE Trans. Geosci. Remote Sens.*, vol. 41, no. 1, pp. 4–19, Jan. 2003.

[14] L. Torres, S. J. S. Sant'Anna, C. da Costa Freitas, and A. C. Frery, "Speckle reduction in polarimetric SAR imagery with stochastic distances and nonlocal means," *Pattern Recognit.*, vol. 47, no. 1, pp. 141–157, Jan. 2014.

[15] G. Liu and H. Zhong, "Nonlocal means filter for polarimetric SAR data despeckling based on discriminative similarity measure," *IEEE Geosci. Remote Sens. Lett.*, vol. 11, no. 2, pp. 514–518, Feb. 2014.

[16] M. Elad and M. Aharon, "Image denoising via sparse and redundant representations over learned dictionaries," *IEEE Trans. Image Process.*, vol. 15, no. 12, pp. 3736–3745, Dec. 2006.

[17] J. Mairal, M. Elad, and G. Sapiro, "Sparse representation for color image restoration," *IEEE Trans. Image Process.*, vol. 17, no. 1, pp. 53–69, Jan. 2008.

[18] J. Mairal, F. Bach, J. Ponce, G. Sapiro, and A. Zisserman, "Non-local sparse models for image restoration," in *Proc. IEEE Int. Conf. Comput. Vis.*, 2009, pp. 2272–2279.

[19] S. Foucher, "SAR image filtering via learned dictionaries and sparse representations," in *Proc. IEEE Int. Geosci. Remote Sens. Symp.*, 2008, vol. 1, pp. 229–232.

[20] J. Jiang, L. Jiang, and N. Sang, "Non-local sparse models for SAR image despeckling," in *Proc. IEEE Int. Conf. Comput. Vis. Remote Sens.*, 2012, pp. 230–236.

[21] B. Xu *et al.*, "Patch ordering based SAR image despeckling via transform-domain filtering," *IEEE J. Sel. Topics Appl. Earth Observ. Remote Sens.*, vol. 8, no. 4, pp. 1682–1695, Apr. 2015.

[22] I. Ram, M. Elad, and I. Cohen, "Image processing using smooth ordering of its patches," *IEEE Trans. Image Process.*, vol. 22, no. 7, pp. 2764–2774, Jul. 2013.
[23] J. S. Lee and E. Pottier, *Polarimetric Radar Imaging: From Basics to Applications*. Boca Raton, FL, USA: CRC Press, 2009.
[24] N. R. Goodman, "Statistical analysis based on a certain multi-variate complex Gaussian distribution (an introduction)," *Ann. Math. Stat.*, vol. 34, no. 1, pp. 152–177, Mar. 1963.
[25] S. N. Anfinsen, A. P. Doulgeris, and T. Eltoft, "Estimation of the equivalent number of looks in polarimetric synthetic aperture radar imagery," *IEEE Trans. Geosci. Remote Sens.*, vol. 47, no. 11, pp. 3795–3809, Nov. 2009.
[26] J. S. Lee, "Digital image enhancement and noise filtering by use of local statistics," *IEEE Trans. Pattern Anal. Mach. Intell.*, vol. PAMI-2, no. 2, pp. 165–168, Mar. 1980.
[27] V. S. Frost, J. A. Stiles, K. S. Shanmugan, and J. C. Holtzman, "A model for radar images and its application to adaptive digital filtering of multiplicative noise," *IEEE Trans. Pattern Anal. Mach. Intell.*, vol. PAMI-4, no. 2, pp. 157–166, Mar. 1982.
[28] R. J. A. Tough, D. Blacknell, and S. Quegan, "A statistical description of polarimetric and interferometric synthetic aperture radar data," *Proc. R. Soc. Lond. A, Math. Phys. Sci.*, vol. 449, no. 1937, pp. 567–589, Jun. 1995.
[29] J. A. Tropp, "Greed is good: Algorithmic results for sparse approximation," *IEEE Trans. Inf. Theory*, vol. 50, no. 10, pp. 2231–2242, Oct. 2004.
[30] J. A. Tropp, "Algorithms for simultaneous sparse approximation. Part I: Greedy pursuit," *Signal Process.*, vol. 86, no. 3, pp. 572–588, Mar. 2006.
[31] J. A. Tropp, "Algorithms for simultaneous sparse approximation. Part II: Conve relaxation," *Signal Process.*, vol. 86, no. 3, pp. 589–602, Mar. 2006.
[32] J. S. Lee, T. L. Ainsworth, J. P. Kelly, and C. López-Martínez, "Evaluation and bias removal of multi-look effect on entropy/alpha/anisotropy in polarimetric SAR decomposition," *IEEE Trans. Geosci. Remote Sens.*, vol. 46, no. 10, pp. 3039–3052, Oct. 2008.
[33] The Polarimetric SAR Data Processing and Educational Tool. [Online]. Available: http://earth.esa.int/polsarpro.
[34] [Online]. Available: http://oa.ee.tsinghua.edu.cn/%7eyangjian/xubin/code/POLSAR-POSSC-v0.1.zip.
[35] S. Foucher and C. López-Martínez, "Analysis, evaluation, and comparison of polarimetric SAR speckle filtering techniques," *IEEE Trans. Image Process.*, vol. 23, no. 4, pp. 1751–1764, Apr. 2014.
[36] J. Canny, "A computational approach to edge detection," *IEEE Trans. Pattern Anal. Mach. Intell.*, vol. PAMI-8, no. 6, pp. 679–698, Nov. 1986.
[37] G. Di Martino *et al.*, "Benchmarking framework for SAR despeckling," *IEEE Trans. Geosci. Remote Sens.*, vol. 52, no. 3, pp. 1596–1615, Mar. 2014.
[38] F. Argenti, T. Bianchi, and A. Alparone, "Segmentation-based MAP despeckling of SAR images in the undecimated wavelet domain," *IEEE Trans. Geosci. Remote Sens.*, vol. 46, no. 9, pp. 2728–2742, Sep. 2008.
[39] S. Parrilli, M. Poderico, C. V. Angelino, and L. Verdoliva, "A nonlocal SAR image denoising algorithm based on LLMMSE wavelet shrinkage," *IEEE Trans. Geosci. Remote Sens.*, vol. 50, no. 2, pp. 606–616, Feb. 2012.
[40] E. Jakeman and P. N. Pusey, "A model for non-Rayleigh sea echo," *IEEE Trans. Antennas Propag.*, vol. AP-24, no. 6, pp. 806–814, Nov. 1976.
[41] F. Argenti, A. Lapini, T. Bianchi, and L. Alparone, "A tutorial on speckle reduction in synthetic aperture radar images," *IEEE Geosci. Remote Sens. Mag.*, vol. 1, no. 3, pp. 6–35, Sep. 2013.
[42] S. R. Cloude and E. Pottier, "A review of target decomposition theorems in radar polarimetry," *IEEE Trans. Geosci. Remote Sens.*, vol. 34, no. 2, pp. 498–518, Feb. 1996.

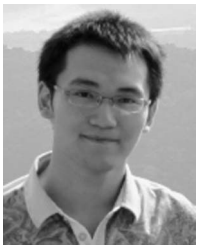

Bin Xu received the B.S. degree from Tsinghua University, Beijing, China, in 2011, where he is currently working toward the Ph.D. degree in the Department of Electronic Engineering.

His research work focuses on SAR image processing and polarimetric SAR image processing.

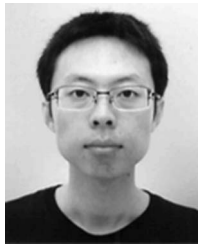

Yi Cui (S'09–M'11) received the B.S. degree (with honors) in electronic information science and technology from Jilin University, Changchun, China, in 2006 and the Ph.D. degree in information and communication engineering from Tsinghua University, Beijing, China, in 2011.

From 2011 to 2014, he was a Postdoctoral Fellow at Niigata University, Niigata, Japan. From 2014 to 2015, he was a Postdoctoral Fellow at Hokkaido University, Sapporo, Japan. Currently, he is a Research Associate at Standford University, CA, USA.

Dr. Cui is an Associate Editor of the IEEE JOURNAL OF SELECTED TOPICS IN APPLIED EARTH OBSERVATION AND REMOTE SENSING. He has been recognized as a 2013 Best Reviewer of the IEEE TRANSACTIONS ON GEOSCIENCE AND REMOTE SENSING. He was the first-prize winner of the student paper competition at the 2010 Asia-Pacific Radio Science Conference (AP-RASC10), the recipient of the Best Paper Award of the 2012 International Symposium on Antennas and Propagation, and the recipient of the 2013 IEEE Geoscience and Remote Sensing Society Symposium Prize Paper Award.

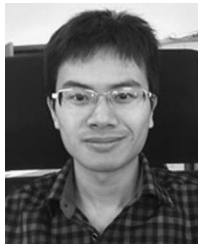

Bin Zuo received the B.S. degree from Tsinghua University, Beijing, China, in 2013, where he is currently working toward the Ph.D. degree in the Department of Electronic Engineering.

His research work focuses on polarimetric SAR image processing.

Jian Yang (M'98–SM'02) received the B.S. and M.S. degrees from Northwestern Polytechnical University, Xian, China, in 1985 and 1990, respectively, and the Ph.D. degree from Niigata University, Niigata, Japan, in 1999.

In 1985, he was with the Department of Applied Mathematics, Northwestern Polytechnical University. From 1999 to 2000, he was an Assistant Professor with Niigata University. In April 2000, he was with the Department of Electronic Engineering, Tsinghua University, Beijing, China, where he is currently a Professor. His research interests include radar polarimetry, remote sensing, mathematical modeling, optimization in engineering, and fuzzy theory.

Dr. Yang is an Associate Editor of the IEEE TRANSACTIONS ON GEOSCIENCE AND REMOTE SENSING, the Vice-Chairman of the IEEE Aerospace and Electronic Systems in the Beijing Chapter, and the former Chairman of the Institute of Electronics, Information and Communication Engineers in Beijing area.

Jianshe Song received the B.S. degree from Shanxi Normal University, Xi'an, China, in 1982 and the M.S. and Ph.D. degrees from Xidian University, Xi'an, in 1989 and 2001, respectively.

He is currently a Professor of the Xi'an Research Institute of Hi-Technology, Xi'an, China. He has finished many projects and received more than ten awards from the Chinese government. He published five books and more than 150 papers. His research interests include radar theory, signal processing, and optimization in engineering.